

Band Artifacts Due to Bulk Motion

Pippa Storey,* Qun Chen, Wei Li, Robert R. Edelman, and Pottumarthi V. Prasad

Band artifacts due to bulk motion were investigated in images acquired with fast gradient echo sequences. A simple analytical calculation shows that the width of the artifacts has a square-root dependence on the velocity of the imaged object, the time taken to acquire each line of k -space and the field of view in the phase-encoding direction. The theory furthermore predicts that the artifact width can be reduced using parallel imaging by a factor equal to the square root of the acceleration parameter. The analysis and results are presented for motion in the phase- and frequency-encoding directions and comparisons are made between sequential and centric ordering. The theory is validated in phantom experiments, in which bulk motion is simulated in a controlled and reproducible manner by rocking the scan table back and forth along the bore axis. Preliminary cardiac studies in healthy human volunteers show that dark bands may be observed in the endocardium in images acquired with nonsegmented fast gradient echo sequences. The fact that the position of the bands changes with the phase-encoding direction suggests that they may be artifacts due to motion of the heart walls during the image acquisition period. Magn Reson Med 48:1028–1036, 2002. © 2002 Wiley-Liss, Inc.

Key words: MRI; motion artifacts; parallel imaging; phase-encoding order; myocardium

In the present study, we investigated the effect of translational motion between successive phase-encoding steps in fast gradient-echo sequences. Such sequences are conventionally used in first-pass myocardial perfusion MRI (1), which requires high temporal resolution (typically one heartbeat). The motivation for this study was our observation of dark bands in the endocardium of apparently healthy control subjects undergoing perfusion scans. We hypothesized that the bands were artifacts due to motion of the heart walls during the acquisition period. As a first step in testing this hypothesis, we developed a theoretical model to predict the effects of motion in the phase- and frequency-encoding directions and validated the theory in phantom experiments in which tissue motion is simulated in a controlled and reproducible manner, using the “rocker” feature available on the GE Medical Systems (Milwaukee, WI) CV/i scanner. We also present the results of preliminary cardiac studies in healthy human volunteers. The images exhibit dark bands in the endocardium, whose location and size are consistent with the hypothesis of bulk motion artifacts. More comprehensive cardiac studies are anticipated to test this hypothesis further.

Department of Radiology, Evanston Northwestern Healthcare, Evanston Illinois, and Northwestern University Medical School, Chicago Illinois.

Grant sponsor: National Institutes of Health; Grant number: HL60708.

*Correspondence to: Pippa Storey, Ph.D., Department of Radiology, MRI Research, Rm. 5108, Evanston Hospital, 2650 Ridge Avenue, Evanston, IL 60201. E-mail: p-storey@northwestern.edu

Received 10 April 2002; revised 10 August 2002; accepted 20 August 2002.

DOI 10.1002/mrm.10314

Published online in Wiley InterScience (www.interscience.wiley.com).

© 2002 Wiley-Liss, Inc.

THEORY

In fast gradient echo sequences, a single line of k -space data is collected for every excitation pulse. It is assumed that the phases imparted by the imaging gradients during the acquisition of one line do not corrupt those of the next. This is ensured by the use of gradient or RF spoiling. Under this condition, each k -space line can be considered independently of the others, since it is sensitive only to the position of the imaged tissue at the time that line is acquired and is unaffected by the details of the motion up to that point. Furthermore, for the tissue velocities typically encountered in cardiac imaging, we can, to a good approximation, neglect the motion that occurs during the acquisition of a single line, both during the time between the RF excitation and the signal readout and during the readout period itself. Only motion that occurs between successive phase-encoding steps need be considered. In the terminology of Xiang and Henkelman (2), we can neglect “intra-view” effects and consider only “inter-view” effects.

Theoretical Model

We begin by considering motion in the phase-encoding direction. This is the simplest case to treat analytically, since it can be described in one dimension. Let x denote position, and let k be the corresponding dimension in k -space. Without loss of generality we will consider uniform motion of the imaged structures. Due to the linearity of the Fourier transformation, which underlies the image reconstruction procedure, the extension to multiple objects moving independently and undergoing distortion is trivial.

The case of a nonsegmented acquisition with sequential phase ordering can be treated analytically, and we will consider this situation first. Assuming constant velocity v , adjacent lines of k -space will be collected with the object at incrementally different positions. A displacement Δx_j in image space corresponds to multiplication in k -space by a phase “twist”:

$$\varphi(k_j) = \exp(-ik_j\Delta x_j), \quad [1]$$

where $k_j = j\delta k$ denotes the j th line in k -space and δk is the increment between adjacent phase-encoding lines, which is related to the field of view (FOV) X_{ph} in the phase-encoding direction by:

$$\delta k = \frac{2\pi}{X_{ph}}. \quad [2]$$

The index j ranges from $-N/2$ to $N/2-1$, where N is the number of phase encoding lines. Since the object is moving, the displacement appearing in Eq. [1] also depends on j . For sequential ordering the dependence is linear:

$$\Delta x_j = v\tau j = v\tau \frac{k_j}{\delta k} = \frac{X_{\text{ph}}v\tau k_j}{2\pi}, \quad [3]$$

where τ denotes the time to acquire each phase encoding line, which, for nonsegmented fast gradient echo sequences, equals the repetition time TR. Substituting the value of Δx_j into Eq. [1] gives:

$$\varphi(k_j) = \exp\left(-i \frac{X_{\text{ph}}v\tau k_j^2}{2\pi}\right). \quad [4]$$

The effect of the motion is thus to multiply the k -space signal S by the function φ , giving:

$$S_v = S_0\varphi, \quad [5]$$

where the subscripts 0 and v label the data for the object when it is stationary and when it is moving with velocity v , respectively. In image space, this is equivalent to convolution of the object's intensity profile by the Fourier transform of φ , which we shall denote ψ . The final image is given by:

$$I_v = |\rho_v| = |\rho_0 * \psi|. \quad [6]$$

This result is analogous to that obtained by Wedeen et al. (3), who considered motion during the readout period. The kernel ψ , which determines the form of the artifacts, can be calculated analytically:

$$\psi(x_j) \approx \frac{e^{-i\pi/4}}{N} \sqrt{\frac{X_{\text{ph}}}{2v\tau}} \exp\left(i\pi \frac{x_j^2}{2X_{\text{ph}}v\tau}\right). \quad [7]$$

Note that ψ is an oscillatory function, which increases in frequency away from the origin. Far from tissue boundaries the high-frequency oscillations interfere destructively and the effect of motion on the image is negligible. However, at tissue boundaries the motion results in band artifacts. The length scale of the artifacts is characterized by the width of the central lobe of ψ , namely:

$$\lambda \equiv \sqrt{2X_{\text{ph}}v\tau}. \quad [8]$$

In terms of λ , the function ψ can be written as:

$$\psi(x_{\text{ph}}) \approx e^{-i\pi/4} \frac{X_{\text{ph}}}{N\lambda} \exp\left[i\pi \left(\frac{x_{\text{ph}}}{\lambda}\right)^2\right], \quad [9]$$

where we have dropped the index j on the position x , and replaced it with the subscript “ph” to emphasize that the position is in the phase-encoding direction.

Predictions of the Theory

Figure 1 shows the calculated image profile of a tissue boundary modeled as a step function, moving in the phase-encoding direction, and scanned using a nonsegmented fast gradient echo sequence with sequential phase ordering. Due to the symmetry of the function ψ , the artifacts are independent of the direction of motion. Hence,

Sequential ordering

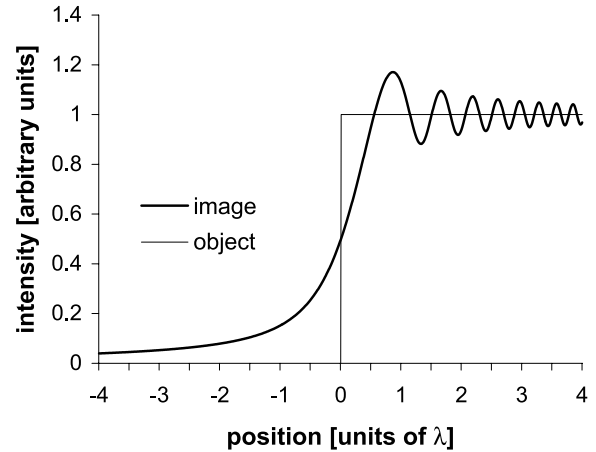


FIG. 1. The intensity profile of a tissue boundary modeled as a step function and moving in the phase-encoding direction. The imaging sequence is assumed to be a nonsegmented fast gradient echo, with sequential ordering. Due to symmetry, the motion could be either to the left or right. The position is shown in units of the characteristic length λ and the width of the first lobe of the oscillations, taken from the point of half-peak intensity to the position of the first dip, is equal to 1.21λ .

the intensity oscillations appearing on the “leading” and “trailing” edges of an object will be mirror images of each other.

Note that since the x -axis in Fig. 1 is plotted in units of λ , the graph applies to any set of parameters X_{ph} , v , and τ . It is instructive, however, to insert some typical values for these parameters to gain an appreciation of the length scales involved and thereby gauge the implications for cardiac imaging. From short-axis cine scans of the heart, we estimate radial velocities of the endocardial border to vary from 0 cm/s at end-diastole and end-systole, to about 7 cm/s during the contraction and filling phases. Typical fields of view in the phase-encoding direction fall in the range 30–40 cm, and fast gradient echo sequences on state-of-the-art scanners have repetitions times on the order of 2–4 ms. Substituting these values into the expression for λ , we find that the length scale of the artifacts can range from 0–1.5 cm, depending on the cardiac phase and the imaging parameters. This is significant both for the design of cardiac MRI protocols and for the diagnostic interpretation of the resulting images.

To compare the predictions of the theory with the results of the phantom experiments, we need to choose two landmarks on the artifacts that will be easy to locate on the images and define an artifact “width” w as the distance between these two points. Because the function ψ scales with the parameter λ , the width w , however it is defined, must be proportional to λ . For convenience we will choose the landmarks to be the point of half-peak intensity and the position of the first dip in the oscillations (see Fig. 1). The value of the width w thus defined can be calculated numerically and equals:

$$w_{\text{sequential}} \approx 1.2122\lambda. \quad [10]$$

The fact that the constant of proportionality is close to unity justifies the description of λ as the “characteristic length scale” of the artifacts. Although the detailed structure of the artifacts depends on the phase-encoding order, the expression for the length scale applies more generally.

Amplitude of the Artifacts

We now calculate the amplitude of the artifacts at a tissue boundary, modeled as a step function:

$$\rho_0(x) = \begin{cases} 0, & x < 0 \\ I_0, & x \geq 0 \end{cases} \quad [11]$$

The intensity profile [6] of the image is given by the convolution of $\rho_0(x)$ with $\psi(x)$:

$$I(x_j) = \left| \sum_{l=-N/2}^{N/2-1} \rho_0(x_j - x_l) \psi(x_l) \right| = I_0 \left| \sum_{l=-N/2}^j \psi(x_l) \right|. \quad [12]$$

In the regime where the length scale of the artifacts is much larger than the size of a single pixel, we can approximate the sum by an integral. Letting the number of phase-encoding lines tend to infinity, $N \rightarrow \infty$:

$$I(x) = I_0 \left| \frac{e^{-i\pi/4}}{\lambda} \int_{-X_{\text{ph}}/2}^x dx' \exp \left[i\pi \left(\frac{x'}{\lambda} \right)^2 \right] \right| = I_0 F(x/\lambda), \quad [13]$$

where, for a large FOV $X_{\text{ph}} \rightarrow \infty$, the function F is:

$$F(u) \equiv \left| e^{-i\pi/4} \int_{-\infty}^u du' \exp(i\pi u'^2) \right|. \quad [14]$$

It is clear from Eqs. [13] and [14] that while the spatial dimensions of the artifacts scale with λ , their amplitude depends only on the signal contrast I_0 at the tissue interface. This result holds provided λ is much greater than the size of a single pixel. In the “slow motion” regime, in which the artifact width is comparable with or smaller than the size of a single pixel, the artifacts will diminish in amplitude or disappear altogether.

Centric Reordering

The phase ordering enters the calculation through the expression for Δx_j , the displacement of the object at the moment that the j th line is acquired. For centric ordering, in which the central line of k -space is collected first, the displacement can be written to a good approximation as $\Delta x_j = 2\nu\tau|j|$. Substituting this expression into Eq. [1] for φ gives:

$$\varphi_{\text{centric}}(k_j) = \exp\left(-i \frac{2\nu\tau k_j |k_j|}{\delta k}\right). \quad [15]$$

The Fourier transform of this function cannot be determined analytically. However, the artifacts that it produces

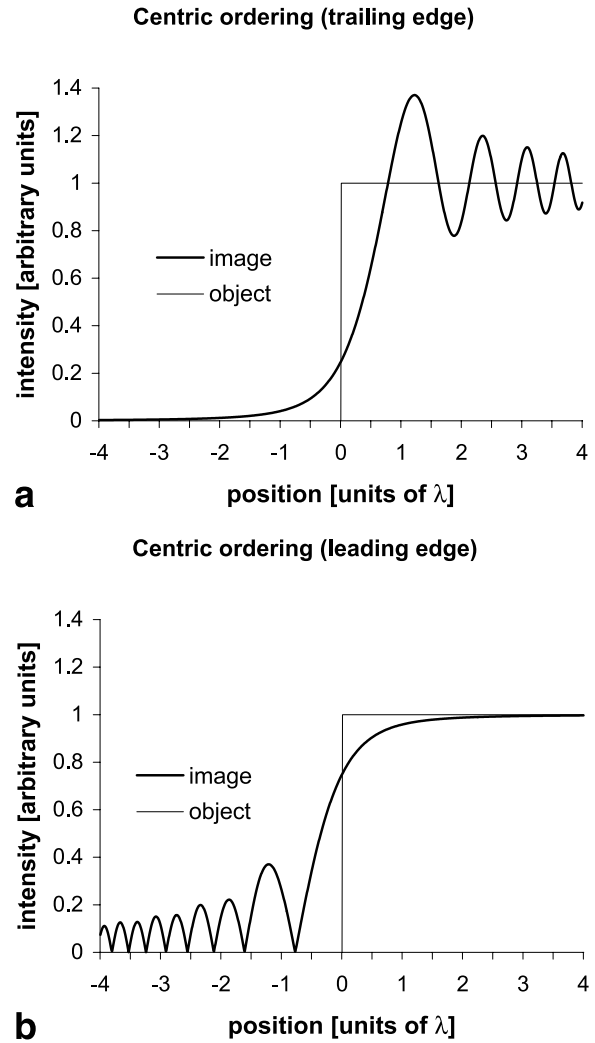


FIG. 2. The intensity profile of a tissue boundary as in Fig. 1 but with centric reordering. Graphs **a** and **b** correspond to motion towards the right and left, respectively. The width of the first lobe of the oscillations on the trailing edge, taken from the point of half-peak intensity to the position of the first dip, is equal to 1.34λ .

can easily be calculated numerically. The resulting image profiles for a tissue boundary modeled as a step function and moving to the right and left are shown in Fig. 2a,b, respectively. Note that the artifacts are no longer symmetric but depend on the direction of motion. The amplitude of the artifacts is higher than for sequential ordering (cf. Fig. 1) and the width of the first lobe (defined as the distance from the point of half-peak intensity to the position of the first dip on the trailing edge) is $w_{\text{centric}} = 1.34\lambda$, making the artifacts slightly broader. Sequential ordering is thus preferable to centric ordering in minimizing motion artifacts. This observation agrees with the results of Nguyen et al. (4), who studied the influence of phase-ordering on the point-spread function in the presence of motion.

Reducing the Artifacts

If the motion is periodic (as in the case of cardiac motion) and time resolution is not critical, an effective way to

reduce or eliminate the band artifacts is to use a segmented acquisition with interleaved phase-ordering. By spreading the data collection over n cycles of the motion, the acquisition time per cycle decreases by a factor of n . This reduces the effective value of τ , the time taken to acquire each phase-encoding line, by the same factor. Since λ has a square-root dependence on τ , the width of the artifacts diminishes by a factor of \sqrt{n} .

Parallel imaging offers an alternative way to reduce the width of the artifacts. In the SMASH formulation (5), only every n th line of k -space is sampled, where n is now the acceleration factor. The values of the data in the intervening lines are estimated from appropriate linear combinations of the separate signals from individual coil elements. The average time taken to acquire each phase-encoding line is thus reduced by a factor of n , and the width τ of the artifacts decreases by a factor of \sqrt{n} .

In the SENSE formulation (6) the result is identical but the interpretation is slightly different. As in the SMASH technique, k -space is traversed with fewer phase-encoding lines (by a factor of the acceleration parameter n). However, the sparse sampling in this case reflects a decrease in the effective FOV. From the relation $\delta k = 2\pi/X_{\text{ph}}$, it is clear that an increase in δk by a factor of n corresponds to a reduction in X_{ph} by the same factor. The essence of the SENSE reconstruction procedure is to use information about the sensitivity profiles of the individual coil elements to “unwrap” the image in this reduced FOV. However in decreasing X_{ph} by a factor of n , the characteristic length scale λ of the artifacts is also reduced by a factor of \sqrt{n} .

Motion in the Frequency-Encoding Direction

When the frequency-encoding axis coincides with the direction of movement, artifacts appear at tissue boundaries that form corners or lie at an oblique angle to the direction of motion. The case of oblique edges can be treated in terms of the “apparent” motion produced in the phase-encoding direction, using the theory developed in the previous section. However, to analyze corners a full two-dimensional analysis is required. Following a method analogous to that presented above, we find that the effect of motion in the frequency-encoding direction is to convolve the (two-dimensional) image intensity profile by the function:

$$\psi(x_{\text{fr}}, x_{\text{ph}}) = \frac{2X_{\text{fr}}X_{\text{ph}}}{N^2\lambda^2} \exp\left(i4\pi \frac{x_{\text{fr}}x_{\text{ph}}}{\lambda^2}\right), \quad [16]$$

where x_{fr} and x_{ph} denote position in the frequency- and phase-encoding directions, respectively, and X_{fr} and X_{ph} are the corresponding fields of view. Note the reappearance of the parameter $\lambda \equiv \sqrt{2X_{\text{ph}}v\tau}$ in the denominator of the exponent (where v now denotes velocity in the frequency-encoding direction). Artifacts arising from motion in the frequency-encoding direction are thus characterized by the same length scale as those resulting from motion in the phase-encoding direction. However, because ψ depends on the positions x_{fr} and x_{ph} only through their product $x_{\text{fr}}x_{\text{ph}}$, the artifacts occur at tissue boundaries that have components in both the phase-encoding and fre-

quency-encoding directions. From symmetry, it is clear that at a 90° corner the artifacts take the form of a series of bright and dark bands aligned along hyperbolic curves. Numerical calculations predict a sharp intensity peak at the corner and a diagonal distance of $w_{\text{freq}} \approx 0.99\lambda$ between this peak and the second broad dip in the oscillations.

MATERIALS AND METHODS

All imaging was performed on a 1.5 T system (CV/i, General Electric Medical Systems, Milwaukee, WI). In the phantom experiments, bulk tissue motion was simulated in a controlled and reproducible manner by rocking the scan table back and forth along the direction of the bore axis using the in-built “rocker” function. A four-element torso phased array coil was used for signal reception in all studies. Images were acquired with a fast gradient echo sequence (bandwidth ± 62.5 kHz) such as is commonly used for first-pass perfusion imaging, but without any preparatory pulses. A low flip angle (10°) was used to avoid steady-state effects and a large matrix size was chosen (256×256) to minimize truncation artifacts. (Note that, according to the theory, the motion artifacts are independent of matrix size.) The repetition time (TR) and the FOV were varied in the ranges 4.3–10 ms and 25–45 cm, respectively, and the echo time TE was set to its minimum value for the given FOV. A thick slice (20 mm) was used to obtain a high SNR. The table velocity was set to its maximum value and the table displacement was chosen to be 78 mm. This was the largest displacement for which no image aliasing occurred for the smallest FOV used (25 cm). The time between successive image acquisitions was fixed to coincide almost exactly with the period of the table motion. This resulted in a “strobe” effect, allowing the variation of the artifacts over the entire rocker cycle to be followed in “slow motion” when viewed in a cine loop.

A rectangular phantom with a square cross section was placed on the moving table with its long axis across the bore. Images were taken in the sagittal plane and the phase-encoding direction was chosen to be either superior/inferior (along the direction of motion) or anterior/posterior (perpendicular to it). Using sequential phase-encoding, the width of the first lobe of the image artifacts was measured over a range of FOVs (25–45 cm) holding the TR constant (at 10 ms) and also over a range of TR values (4.3–10 ms) holding the FOV constant (at 25 cm). Images were also acquired using centric phase-encoding, but no quantitative measurements were made.

Since the velocity of the table varied throughout the rocker cycle, representative images were acquired over the full cycle and the width of the artifacts was determined for each image using customized routines written in MatLab (MathWorks, Cambridge, MA). We report only the largest values (corresponding to the highest velocity, reached in the middle of the rocker cycle).

As in the case of the artifact width measurements, the table velocity was measured throughout the rocker cycle and only the maximum value is reported. The velocity measurements were made by imaging the phantom repeatedly using the same pulse sequence as described above, but minimizing the artifacts at the leading and trailing

edges of the phantom by using a short TR and choosing the phase-encoding direction to be perpendicular to the direction of motion. The period of the table cycle and the delay between successive image acquisitions were measured using a stopwatch and the velocity computed using automated MatLab routines.

Parallel imaging was performed using the SENSE technique (6). In these studies it was important for the accuracy of the coil sensitivity calibration to ensure that the receiver elements remain stationary with respect to the FOV. They could not, therefore, be laid directly on top of or underneath the phantom, which moved with the table. Instead, the coil elements were attached to the top of a sponge mattress pad, which was bent into an arc and fitted inside the bore above the table. The width of the first lobe of the motion artifacts was measured over a range of TR values (4.3–10 ms) holding the FOV constant at 25 cm. This FOV was less than double the width of the phantom (14.8 cm), and hence sufficiently small to test the accuracy of the SENSE reconstruction.

Preliminary cardiac studies were performed in healthy volunteers in accordance with IRB requirements. The same pulse sequence as described above was used but the acquisition was gated to the cardiac cycle and the readout was preceded by a slice-selective inversion pulse (TI = 400 ms) to produce signal contrast between the myocardium and inflowing blood in the ventricular cavity. No exogenous contrast agents were used. An axial slice was prescribed through the left ventricle and two series of images were taken, one with the phase-encoding direction aligned along the anterior/posterior axis and the other with it oriented left/right. An FOV of 30×40 cm was used, with a matrix size of 96×256 . The repetition time was TR = 5.2 ms and the phase-encoding order was centric.

In order to determine the velocity of the endocardial border, a cine series was acquired using a steady-state free precession sequence. The vertical and horizontal motion of the endocardial border was estimated by manual selection of the myocardial–ventricular interface on successive images.

RESULTS

Motion in the Phase-Encoding Direction

With the phase-encoding axis aligned with the direction of motion, band artifacts were observed at the leading and trailing edges of the phantom. Figure 3 shows a typical image and its intensity profile, obtained using sequential ordering. The corresponding results for centric ordering are presented in Fig. 4. Note that while the artifacts on the leading and trailing edges of the phantom in Fig. 3 are symmetric, those of Fig. 4 are not. In each case their form agrees qualitatively with the predictions of the theory (cf. Figs. 1, 2). The fact that the artifacts in Figs. 3 and 4 are markedly different from each other, and that those in Fig. 4 depend on the direction of movement, confirm that they are indeed motion-induced and not due to some other cause such as truncation error or susceptibility variation.

To provide a quantitative test of the theory, the width of the first lobe of the artifacts was measured over a range of FOVs and TR values (Fig. 5a,b, respectively). Sequential

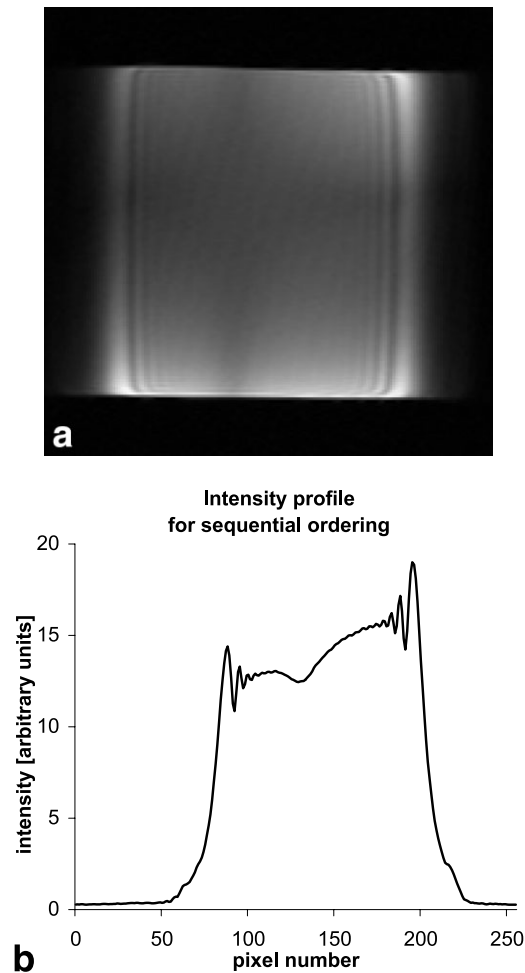


FIG. 3. A typical image (a) and the corresponding intensity profile (b) of a phantom moving in the phase-encoding direction, acquired using sequential phase ordering. Note the symmetrical motion-induced band artifacts on the leading and trailing edges of the phantom (cf. Fig. 1).

phase ordering was used and the width was measured from the point of half-peak intensity to the position of the first dip in the oscillations. The experimental uncertainty in this measurement is estimated, by convention, to be half the maximum error (namely, one pixel) and we have accordingly included error bars of ± 0.5 pixels on the graphs.

Using Eq. [10], the artifact width defined as described above is given by:

$$w = 1.2122 \sqrt{2 \cdot \text{FOV} \cdot v \cdot \text{TR}}, \quad [17]$$

where v is the velocity of the object and the FOV is measured in the phase-encoding direction. In the case of Fig. 5a, only the FOV is varied and the line of best fit can be written as:

$$w = \eta \sqrt{\text{FOV}}, \quad [18]$$

where the theoretical expression for η is:

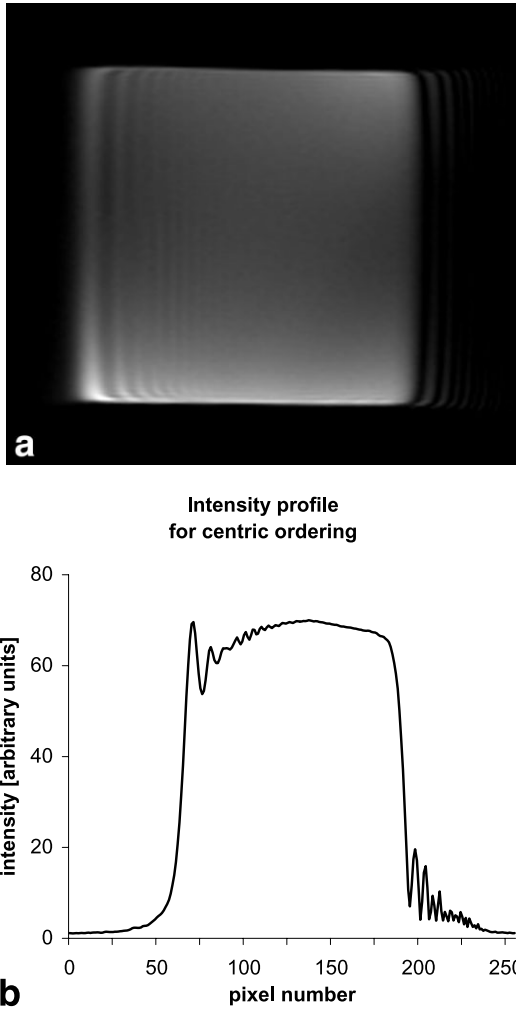


FIG. 4. An image (a) and corresponding intensity profile (b) of a phantom moving towards the right in the phase-encoding direction acquired using centric ordering. Note that the motion artifacts on the leading and trailing edges of the phantom are asymmetric (cf. Fig. 2).

$$\eta = 1.2122 \sqrt{2v \cdot TR}. \quad [19]$$

Table 1 shows the experimentally determined value for η , obtained by fitting the data to a square root curve, and the theoretical value, calculated by substituting into Eq. [19] the values of TR (10 ms) and the table velocity ($v = 6.3 \pm 0.4$ cm/s). Note that the experimental and theoretical values agree to within the margins of uncertainty.

In Fig. 5b the TR is varied and the line of best fit is described by:

$$w = \chi \sqrt{TR}, \quad [20]$$

where the constant of proportionality χ can be expressed as:

$$\chi = 1.2122 \sqrt{2 \cdot FOV \cdot v}. \quad [21]$$

Once again, the experimental and theoretical values for χ (shown in Table 1) agree to within the accuracies of the measurements.

Motion in the Frequency-Encoding Direction

Figure 6 shows a typical image acquired using sequential ordering, with the frequency-encoding axis aligned with the direction of motion. Note the band artifacts at the corners of the phantom, which are symmetric on the leading and trailing edges. Figure 7a,b shows the width of the artifacts as a function of the FOV and the repetition time, respectively. The width is measured along a diagonal line through the corner of the phantom, from the sharp intensity peak to the second broad dip in the oscillations. According to the theory developed above, the width defined in this way is given by:

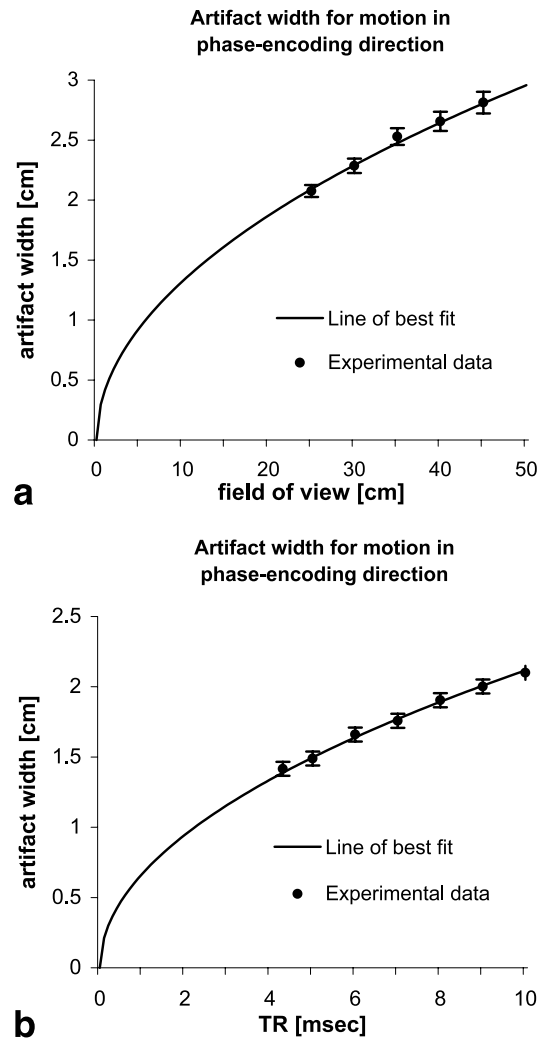


FIG. 5. The width w of the first lobe of the motion artifacts for a phantom moving in the phase-encoding direction and imaged using sequential ordering. The width is plotted as a function of the FOV (a) and the TR value (b). In graph a the TR was held constant at 10 ms and in graph b the FOV was fixed at 25 cm. The error bars are ± 0.5 pixels. The line of best fit in each case is a square root function with one fitted parameter, namely, the constant of proportionality.

Table 1
Theoretical and Experimental Values of η and χ

Direction of motion	Standard reconstruction		SENSE reconstruction
	Varying FOV	Varying TR	Varying TR
Phase-encoding axis	$\eta_{\text{fit}} = 0.418 \pm 0.004\sqrt{\text{cm}}$ $\eta_{\text{th}} = 0.429 \pm 0.015\sqrt{\text{cm}}$	$\chi_{\text{fit}} = 0.670 \pm 0.006 \text{ cm}/\sqrt{\text{ms}}$ $\chi_{\text{th}} = 0.679 \pm 0.024 \text{ cm}/\sqrt{\text{ms}}$	$\chi_{\text{fit}} = 0.460 \pm 0.011 \text{ cm}/\sqrt{\text{ms}}$ $\chi_{\text{th}} = 0.480 \pm 0.017 \text{ cm}/\sqrt{\text{ms}}$
Frequency-encoding axis	$\eta_{\text{fit}} = 0.387 \pm 0.007\sqrt{\text{cm}}$ $\eta_{\text{th}} = 0.351 \pm 0.013\sqrt{\text{cm}}$	$\chi_{\text{fit}} = 0.637 \pm 0.010 \text{ cm}/\sqrt{\text{ms}}$ $\chi_{\text{th}} = 0.554 \pm 0.021 \text{ cm}/\sqrt{\text{ms}}$	

Constants of proportionality η and χ , relating the width of the artifacts to the square root of the FOV and the repetition time TR, respectively. The experimental values, obtained by fitting the data of Figures 5, 7, and 8 to a square root function, are compared with the predicted values, obtained by substituting the measured table velocity into the appropriate theoretical expression.

$$w = 0.99 \sqrt{2 \cdot \text{FOV} \cdot v \cdot \text{TR}}. \quad [22]$$

The data in Fig. 7a,b show in each case a good fit to a square root function. However, the fitted values for the constants of proportionality η and χ are significantly higher than the theoretical values (see Table 1). As discussed below, we believe that the discrepancy results from the fact that the corners of the phantom are not perfectly sharp, as was assumed in the theory.

Application of Parallel Imaging

With the phase-encoding axis coincident with the direction of motion, images were acquired over a range of TR values, using the same parameters as in Fig. 5b, but with SENSE reconstruction at an acceleration factor of two. The results are shown in Fig. 8. As an aid to the eye, we have reproduced the line of best fit from Fig. 5b on the graph. It is clear that the artifact widths obtained using SENSE reconstruction are uniformly lower than those produced using standard reconstruction. The constant of proportionality for the line of best fit to the SENSE data is given in Table 1 and is smaller than the corresponding value for standard reconstruction by a factor of:

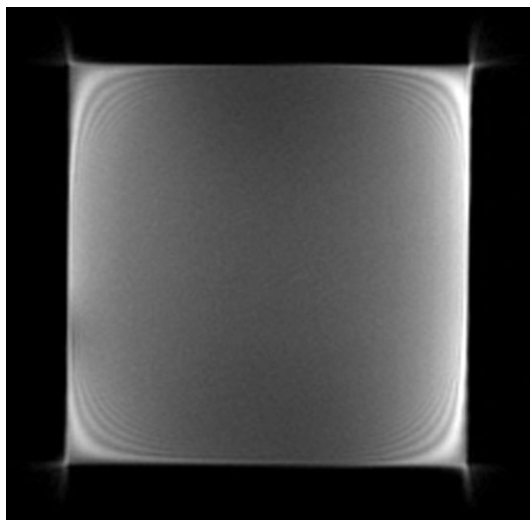


FIG. 6. A phantom moving in the frequency-encoding direction, imaged using sequential phase ordering.

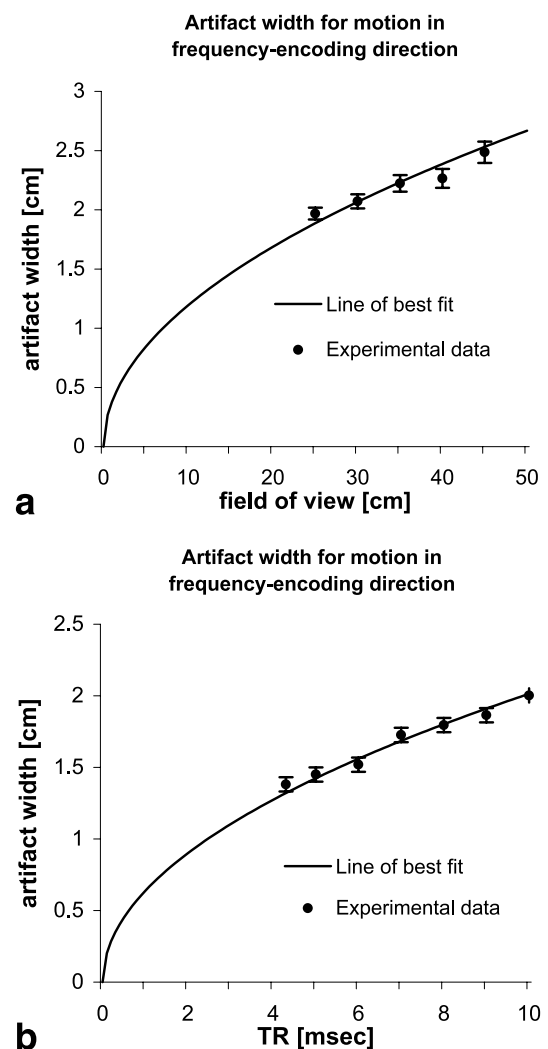


FIG. 7. The width of the motion artifacts for a phantom moving in the frequency-encoding direction and imaged using sequential ordering. The width is evaluated along a diagonal from the corner of the phantom to the second broad dip in the oscillations and is plotted as a function of the FOV (a) and the TR value (b). In graph a the TR was held constant at 10 ms and in graph b the FOV was fixed at 25 cm. The error bars are ± 0.5 pixels. The line of best fit in each case is a square root function with one fitted parameter, namely, the constant of proportionality.

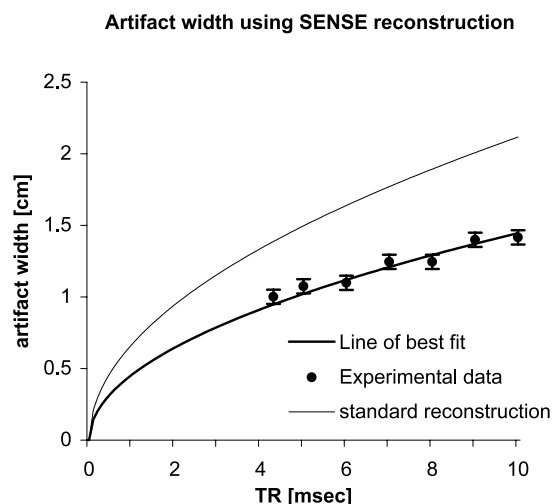


FIG. 8. The width w of the first lobe of the motion artifacts for a phantom moving in the phase-encoding direction, imaged using sequential ordering and SENSE reconstruction, with an acceleration factor of two. The widths are plotted as a function of the TR value, with the FOV fixed at 25 cm. The error bars are ± 0.5 pixels. For comparison, the graph also displays the line of best fit from Fig. 5b, acquired with identical parameters but standard reconstruction.

$$\frac{\chi_{\text{standard}}}{\chi_{\text{SENSE}}} = 1.457 \pm 0.037. \quad [23]$$

Note that the ratio equals the square root of the acceleration factor, namely $\sqrt{2} \approx 1.4142$, to within the experimental uncertainty.

Preliminary Cardiac Studies

Figure 9 shows representative images taken from a healthy volunteer in an axial plane through the left ventricle using centric ordering. In acquiring the left image, the phase-encoding direction was chosen to be anterior/posterior and in obtaining the right image the phase-encoding direction was swapped so that it was oriented left/right. (Note that the phase-encoding direction is clearly evident in each image from the partial aliasing.) In both images, dark bands are visible in the endocardium. However, the location of the bands differs between the two images, being

most prominent on the anterior and posterior borders of the myocardium in the left image and on the left and right borders in the right image. This is consistent with the hypothesis that the bands are motion artifacts, since they appear in the phase-encoding direction.

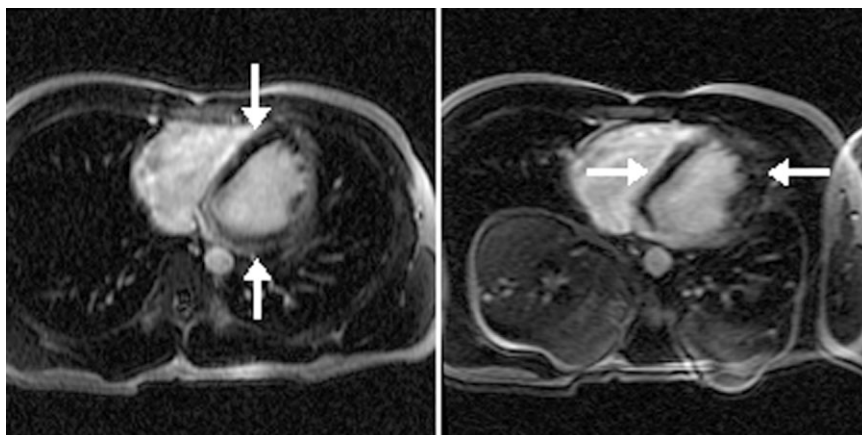
Both the vertical width of the dark bands in the left image and the horizontal width of those in the right image are approximately $w \approx 0.6 \pm 0.1$ cm. We can compare this value with the characteristic length scale of the artifacts predicted from the theory. Cine images were used to estimate the horizontal and vertical velocities of the endocardial border at the relevant cardiac phase. The values could be determined only roughly and were $v_{\text{horiz}} \approx 1.8 \pm 0.6$ cm/s and $v_{\text{vert}} \approx 1.2 \pm 1.2$ cm/s, respectively. Given that the FOV in the phase-encoding direction was 30 cm and the repetition time was 5.2 ms, the theory predicts motion artifacts with length scales of $\lambda \approx 0.7 \pm 0.1$ cm in the horizontal direction and $\lambda \approx 0.6 \pm 0.4$ cm in the vertical direction. These values agree with the width of the dark bands observed in the images to within the experimental uncertainties. While the measurements are only approximate, the agreement supports the hypothesis that the observed bands are due to cardiac motion.

DISCUSSION

This work was motivated by an interest in understanding the effects of cardiac motion in myocardial perfusion imaging. In order to follow the dynamics of the first pass of the contrast agent, perfusion images are typically acquired with a temporal resolution of one heartbeat, using a fast gradient echo sequence. In the present study, we developed a theoretical model to describe the motion artifacts produced by such sequences and validated the theory in a controlled setting using phantom experiments. We have shown that bulk motion of an object causes pronounced band artifacts at tissue boundaries and that the width of the artifacts has a square root dependence on the velocity of the motion, the FOV of the image in the phase-encoding direction, and the repetition time TR between successive phase-encoding steps. It is furthermore demonstrated that parallel imaging reduces the artifact width by a factor equal to the square root of the acceleration parameter.

When motion occurs along the phase-encoding direction, band artifacts are observed on the leading and trailing

FIG. 9. Axial images from a healthy volunteer, with the phase-encoding direction anterior/posterior (left) and left/right (right). The sequence used consists of a slice-selective inversion pulse ($T_I = 400$ ms), to produce signal contrast between the blood and myocardium, followed by a nonsegmented fast gradient-echo readout, identical to that used in the phantom studies. No exogenous contrast material was used. The repetition time was $TR = 5.2$ ms and the phase ordering was centric. Note that in both images dark bands appear in the endocardium (white arrows) and the location of the bands changes with the phase-encoding direction.



edges of the imaged structures. Motion along the frequency-encoding direction produces artifacts on boundaries such as corners and oblique edges, which have components in both the frequency- and phase-encoding directions. The widths of the artifacts we observed on the edges of a phantom moving in the phase-encoding direction agree with the theoretical values to within experimental uncertainty. However, the artifacts appearing at the corners of a phantom moving in the frequency-encoding direction were slightly broader than predicted. We believe the discrepancy is due to the fact that the corners of the phantom were slightly rounded, rather than being perfectly sharp, as was assumed in the theoretical model. Numerical simulations confirm that this causes a broadening of the artifacts.

While we have limited our investigation to motion in the phase- and frequency-encoding directions, through-plane motion is also of interest in cardiac imaging. When a short-axis slice is chosen through the left ventricle, the apparent variation in the diameter of the ventricular cavity over the course of the cardiac cycle is due not only to radial motion of the heart walls (true in-plane motion), but also to motion of the apex with respect to the base (through-plane motion). In terms of the artifacts produced, only the resultant *apparent in-plane motion* is important and this can be treated using the theory developed above.

Preliminary cardiac studies performed in healthy volunteers using a nonsegmented fast gradient echo sequence exhibit dark bands in the myocardium. The fact that the location of the bands changes when the phase-encoding direction is swapped indicates that they are image artifacts. Furthermore, their width is consistent with the hypothesis that they are caused by motion of the heart walls. It remains, however, to determine whether such artifacts appear consistently in cardiac images acquired with nonsegmented fast gradient echo sequences and to prove conclusively that they are due to cardiac motion. This will be the topic of future studies.

Much of the investigation of motion artifacts to date has focused on periodic variations (such as pulsatile flow), in which the acquisition covers several cycles of the motion (7). The ghosting artifacts produced under such conditions can be reduced or eliminated by means of averaging (8), "pseudo-gating" (9), phase-cancellation (10), or phase-reordering (11). Since first-pass myocardial perfusion imaging requires each frame to be acquired within a single cardiac cycle, the techniques designed for periodic motion are not applicable to this situation. An alternative method, involving the acquisition of the central lines of k -space during the quiescent mid-diastolic period (12) is useful for

segmented 3D cardiac imaging but cannot be readily adapted to nonsegmented multislice 2D imaging, since not all the slices can be acquired during mid-diastole. Neither are the methods suggested by Welch et al. (13) and Macgowan and Wood (14) readily applicable to cardiac imaging, since the former corrects only for rigid motion and the latter requires a detailed a priori knowledge of the movement. The most promising avenue for reducing bulk motion artifacts in myocardial perfusion imaging may be to shorten the acquisition time using techniques such as parallel imaging.

ACKNOWLEDGMENTS

We thank Dr. Jason Polzin (GE Medical Systems) for informing us of the "rocker" feature on the GE CV/i scanner. We also thank Dr. Thomas Foo (GE Medical Systems) for writing an inversion-recovery multiphase gradient-echo sequence on which the sequences used here were based.

REFERENCES

1. Wilke NM, Jerosch-Herold M, Zenovich A, Stillman AE. Magnetic resonance first-pass myocardial perfusion imaging: clinical validation and future applications. *J Magn Reson Imag* 1999;10:676–685.
2. Xiang Q-S, Henkelman RM. k -Space description for MR imaging of dynamic objects. *Magn Reson Med* 1993;29:422–428.
3. Wedeen VJ, Wendt RE, Jerosch-Herold M. Motional phase artifacts in Fourier transform MRI. *Magn Reson Med* 1989;11:114–120.
4. Nguyen TD, Ding G, Watts R, Wang Y. Optimization of view ordering for motion artifact suppression. *Magn Reson Imag* 2001;19:951–957.
5. Sodickson DK, Manning WJ. Simultaneous acquisition of spatial harmonics (SMASH): fast imaging with radiofrequency coil arrays. *Magn Reson Med* 1997;38:591–603.
6. Pruessmann KP, Weiger M, Scheidegger MB, Boesiger P. SENSE: sensitivity encoding for fast MRI. *Magn Reson Med* 1999;42:952–962.
7. Wood ML, Henkelman RM. MR image artifacts from periodic motion. *Med Phys* 1985;12:143–151.
8. Dixon WT, Brummer ME, Malko JA. Acquisition order and motional artifact reduction in spin warp images. *Magn Reson Med* 1988;6:74–83.
9. Haacke EM, Lenz GW, Nelson AD. Pseudo-gating: elimination of periodic motion artifacts in magnetic resonance imaging without gating. *Magn Reson Med* 1987;4:162–174.
10. Xiang QS, Bronskill MJ, Henkelman RM. Two-point interference method for suppression of ghost artifacts due to motion. *J Magn Reson Imag* 1993;3:900–906.
11. Haacke EM, Patrick JL. Reducing motion artifacts in two-dimensional Fourier transform imaging. *Magn Reson Imag* 1986;4:359–376.
12. Wang Y, Winchester PA, Yu L, Watts R, Ding G, Lee HM, Bergman GW. Breath-hold three-dimensional contrast-enhanced coronary MR angiography: motion-matched k -space sampling for reducing cardiac motion effects. *Radiology* 2000;215:600–607.
13. Welch EB, Felmler JP, Ehman RL, Manduca A. Motion correction using the k -space difference of orthogonal acquisitions. *Magn Reson Med* 2002;48:147–156.
14. Macgowan CK, Wood ML. Phase-encode reordering to minimize errors caused by motion. *Magn Reson Med* 1996;35:391–398.